Supplementary Information

Section 1: Micro-computed Tomography Data Analysis

Branching of cardiac vasculature. It has been shown that the complex branching geometry of coronary vasculature demonstrates power law scaling as a consequence of the minimization of the cost of construction of the tree structure vs. the cost of operation of fluid flow. Furthermore, existing morphometric data confirm that vascular trees (coronary, pulmonary, muscular) in various species (rat, cat, rabbit, human) obey a set of common design rules resulting in universal power law scaling.

Cardiac vasculature size measurements. The distribution p(R) of vessel radii R is obtained from high-resolution micro-CT measurements of ventricular and atrial tissue using a contrast agent (Microfil, Flow Tech Inc., USA). Figure S1 a) shows a typical reconstruction of a two-dimensional cross section of canine right atrium. Due to their enhanced contrast, cross-sections of the vessels appear as bright spots. Threshold segmentation is used to separate vascular structures from tissue and background regions. The result of the image segmentation is shown in Fig. S1 b). Blob-like artifacts adjacent to the vascular tree occurred due to leakage of contrast agent into the tissue and were removed from the data set. The centerlines of the vessels were approximated in the segmented (i.e., binary) data using morphological operations. The resulting skeleton lines are illustrated in Fig. S1 c). For each voxel of the skeleton tree, the tangential direction was computed. The vessel radii were obtained in a plane perpendicular to this direction using grayscale intensity profiles shown in Figs. S1 e) and f). The intensity profile $I(r)$ of a vessel with radius R is approximated by

$$I(r) = \begin{cases} b + a & \text{for } |r| < r_0 \\ b + a\exp(-\dfrac{(r_0 - r)^2}{2s^2}) & \text{for } |r| \geq r_0 \end{cases}, \qquad \text{(S1)}$$

where b is the background intensity (c.f. Fig. S2). At the center of the vessel, the intensity is assumed to be at a constant value a above the background within a region of size $2r_0$, while the drop-off near the boundary is characterized by s. The approximation of the vessel radius is then given by $R = r_0 + s$ and averaged over intensity profiles at 0, 45, 90, and 135 degrees. The

radius measurement has been calibrated using cylindrical phantoms of known radius. We found that the accuracy for the measurement of vessel radii is 25 μm.

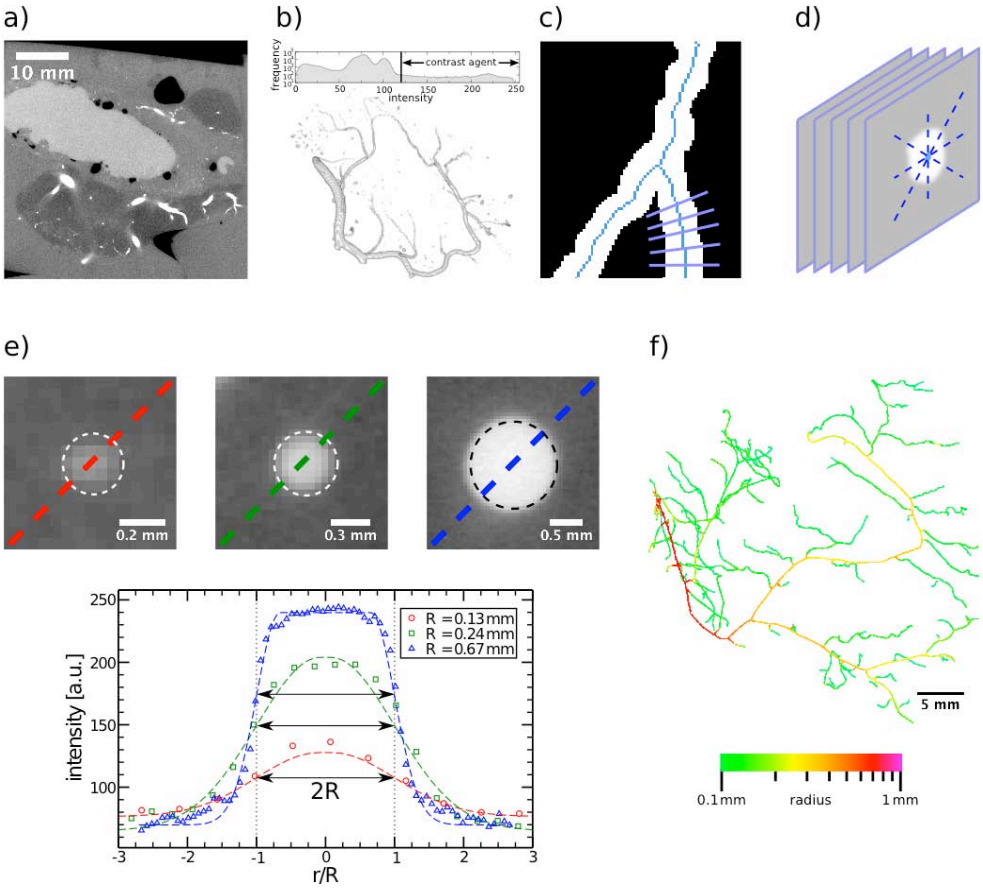

Figure S1: Cardiac Vasculature Size Measurements. a) Unprocessed (raw) micro-CT grayscale image of the canine right atria obtained using contrast agent (MicroFil, Flow Tech Inc., USA) injected into the coronary arteries. Cross-sections of blood vessels filled with contrast agent appear bright. The atrial cavum is filled with silicone (light gray) to preserve its morphology during data acquisition. Air-filled cavities and background appear black. **b)** Approximated vascular tree obtained from the segmentation of two-dimensional slices (c.f. panel a)). **c)** Schematic of the vessel centerline approximation c(x,y,z) based on the binary data obtained in b) using morphological operators (skeletonization; two-dimensional illustration only). The blue lines indicate the positions of cross-sections perpendicular to the centerline. **d)** Two-dimensional gray-scale cross-sections perpendicular to the centerline obtained at each voxel of c(x,y,z). The dashed lines indicate the orientation of one-dimensional intensity profiles at 0, 45, 90, and 135 degrees. **e)** Illustration of the least squares approximation of vascular radii from intensity profiles using Eq. S1 (bottom; c.f. panel d) and Fig. S2). The white and black dashed

lines indicate the approximated radii, i.e., R = 0.13 mm, R = 0.24 mm, and R = 0.67 mm (top row). **f)** Example of a three-dimensional tree-like vascular structure with color-coded vessel radii.

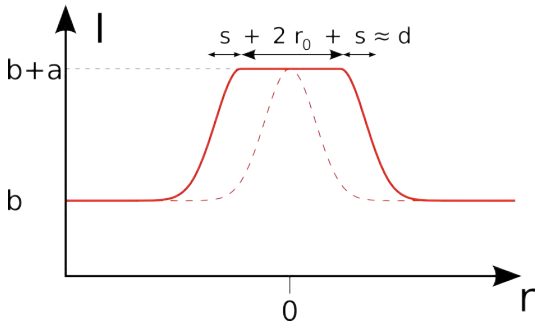

Figure S2: Intensity Profile I(R) of Vessel with Radius R. The radial intensity profile of a vessel is approximated from micro-CT data using Eq. S1, where b is the background intensity and b+a is the intensity at the center of the vessel. In this approximation the radius is given by $R = r_0 + s$.

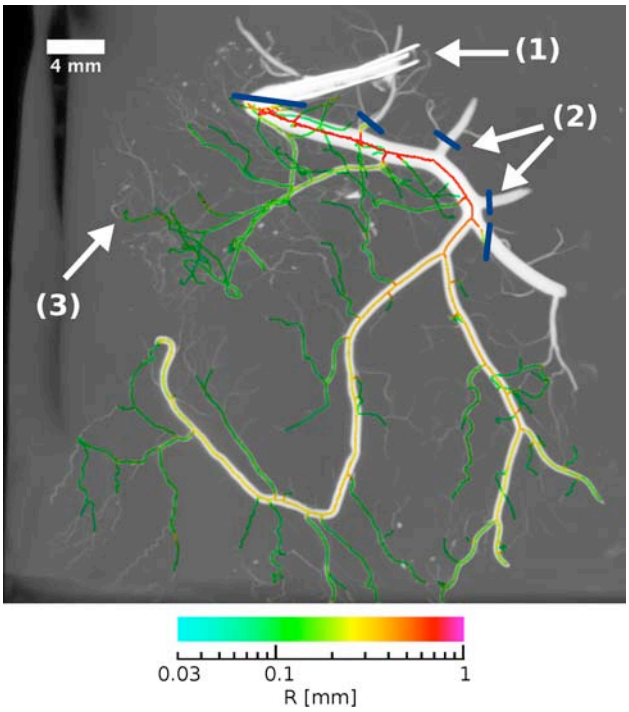

Figure S3: Measurement of Coronary Artery Size. Result of the size measurement (color) is overlaid on the maximum intensity projection of the (unprocessed) micro-CT data (grayscale). The contrast agent (MicroFil, Flow Tech, USA) was injected into the cannula used to perfuse the

tissue (1). Branches (2) that do not perfuse the atrium were excluded from analysis when measuring the atrial size distribution (indicated by blue lines). The smallest measured vessel diameter was 0.03 mm; smaller vessels (3) could not be reliably detected.

Size Distributions Measurements. Size distributions $p(R)$ were obtained from micro-CT measurements using the experimental protocols and data processing algorithms described above. The scaling exponents $p(R) \propto R^{\alpha}$ were estimated using a least squares fit. In atria, we find a scaling exponent α = -2.74 ± 0.05 (N=3). In ventricles, the corresponding exponent is α = -2.75 ± 0.30 (N=3). Statistical analysis showed no significant difference in the scaling exponents for atria and ventricles (P>0.05; see Fig. S4). The size distributions $p(R)$ for individual atrial and ventricular preparations are shown in Figs. S5 and S6, respectively, the corresponding exponents are summarized in the Tables S1 and S2.

Preparation	α_{atrium} [mean ± standard error]
#1	-2.80 ± 0.23
#2	-2.74 ± 0.41
#3	-2.76 ± 0.17
#4	-2.67 ± 0.15
#5	-2.79 ± 0.25
$\overline{\alpha_{atrium}}$	**-2.74 ± 0.05**

Table S1: Scaling Exponents of Size Distributions (Atria). The scaling exponent $\overline{\alpha_{atrium}}$ is the weighted average of exponents for N=5 atrial preparations.

Preparation	[mean ± standard error]
#1	-2.49 ± 0.11
#2	-2.73 ± 0.10
#3	-3.09 ± 0.13
$\overline{\alpha_{ventricle}}$	**-2.75 ± 0.30**

Table S2: Scaling Exponents of Size Distributions (Ventricles). The scaling exponent $\overline{\alpha_{ventricle}}$ is the weighted average of exponents for N=3 ventricular preparations.

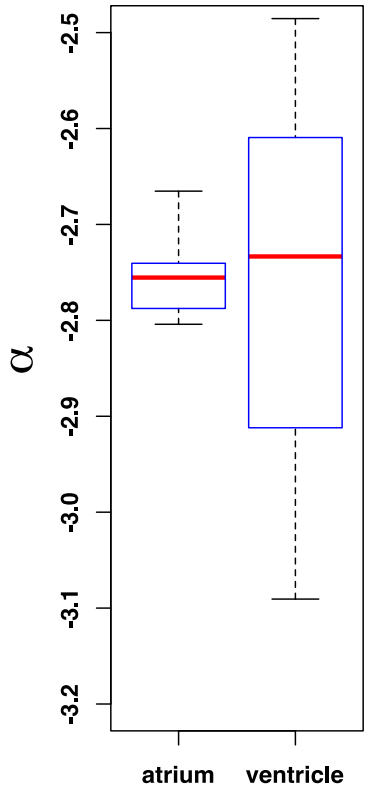

Figure S4: Scaling Exponents α for Atrium and Ventricle. The box plot shows median, the 25th and 75th percentiles. The whiskers indicate the statistically significant data range. Statistical analysis showed no significant difference in the scaling exponents for atria and ventricles (P>0.05).

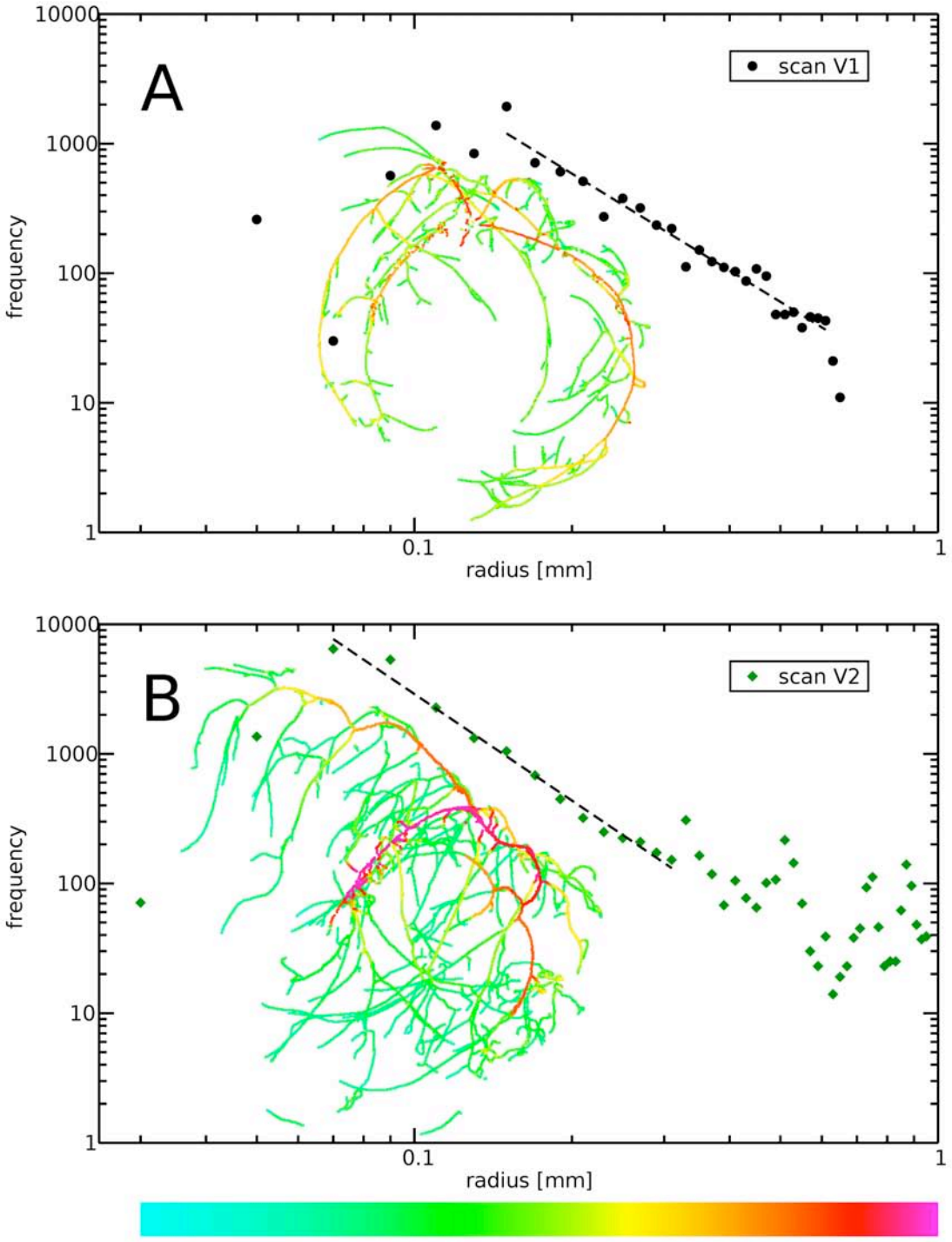

Figure S5: Size Distribution of Cardiac Vasculature (Ventricles).

A $\alpha = -2.49 \pm 0.11$ **B** $\alpha = -2.73 \pm 0.10$ Color bar applies to both panels and indicates radius from 0.03 to 1 mm.

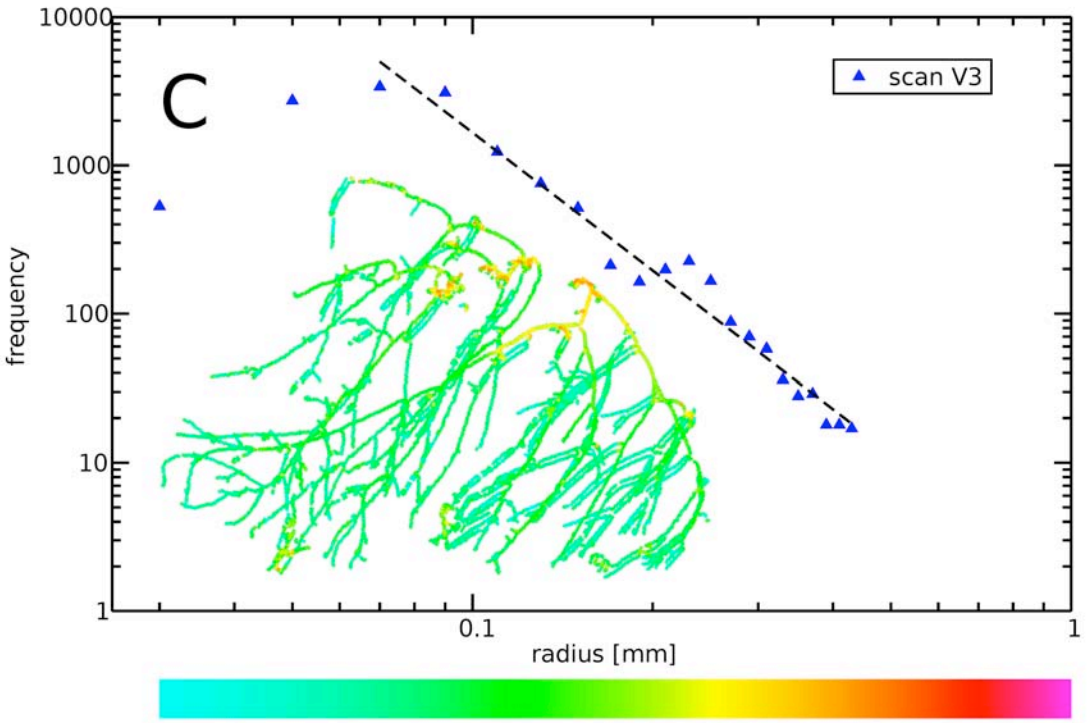

Figure S5: Size Distribution of Cardiac Vasculature (Ventricles) *(continued).*

C $\alpha = -3.09 \pm 0.13$. Color bar applies to all panels and indicates radius from 0.03 to 1 mm.

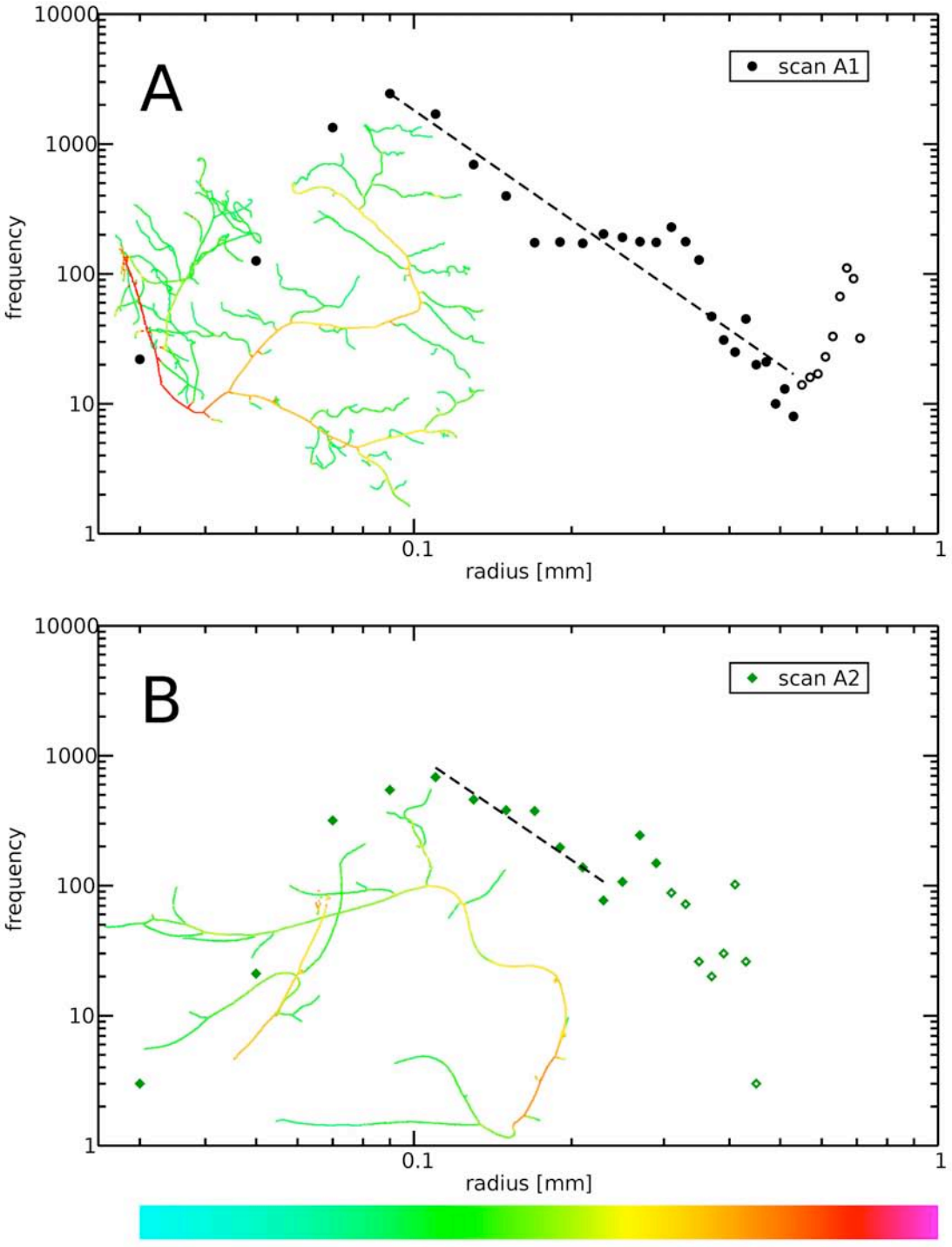

Figure S6: Size Distribution of Cardiac Vasculature (Atria).

A $\alpha = -2.80 \pm 0.23$ **B** $\alpha = -2.74 \pm 0.41$ Color bar applies to both panels and indicates radius from 0.03 to 1 mm. Open symbols indicate data that do not belong to atrial vasculature.

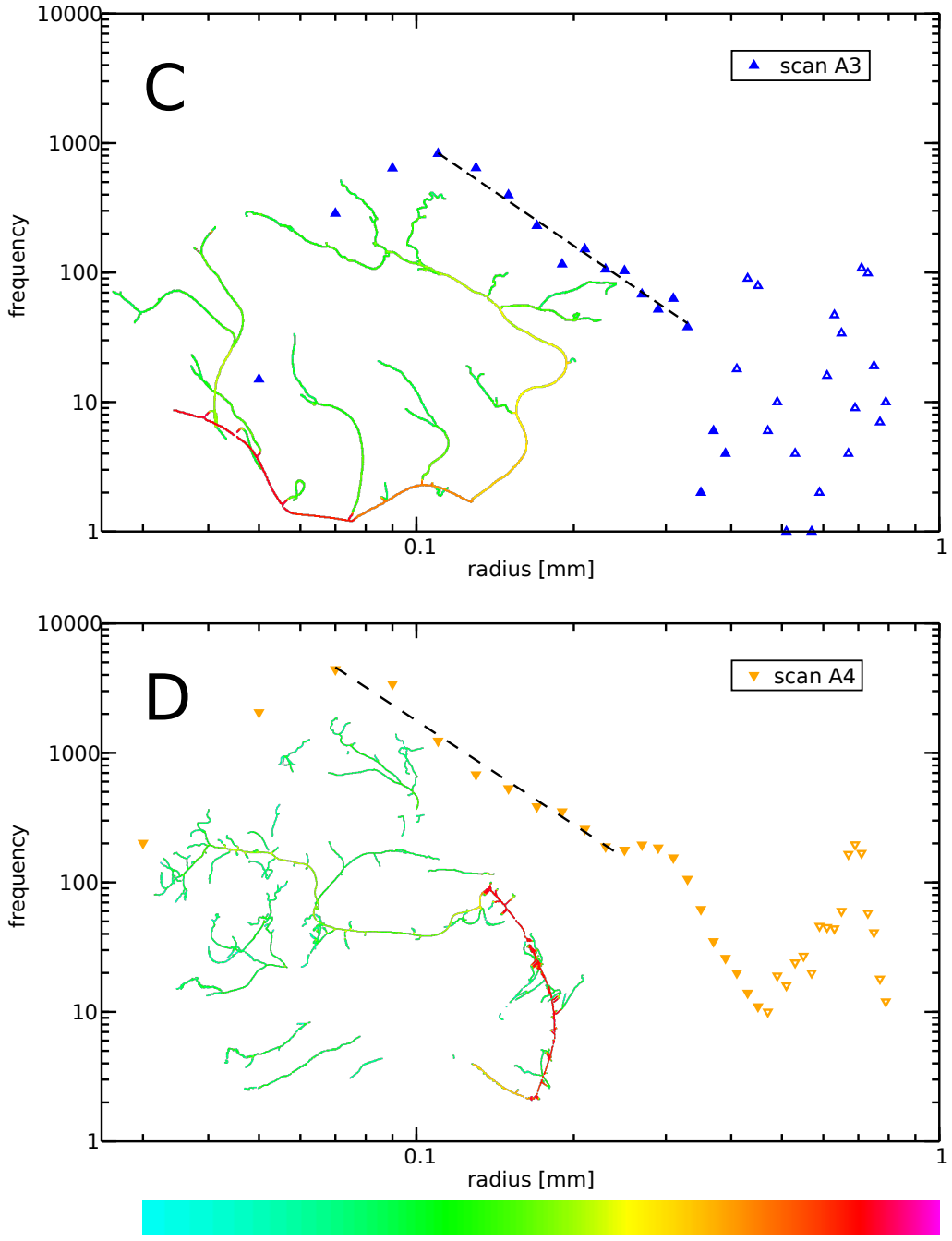

Figure S6: Size Distribution of Cardiac Vasculature (Atria) *(continued).*

C $\alpha = -2.76 \pm 0.17$ **D** $\alpha = -2.67 \pm 0.15$ Color bar applies to both panels and indicates radius from 0.03 to 1 mm. Open symbols indicate data that do not belong the atrial vasculature.

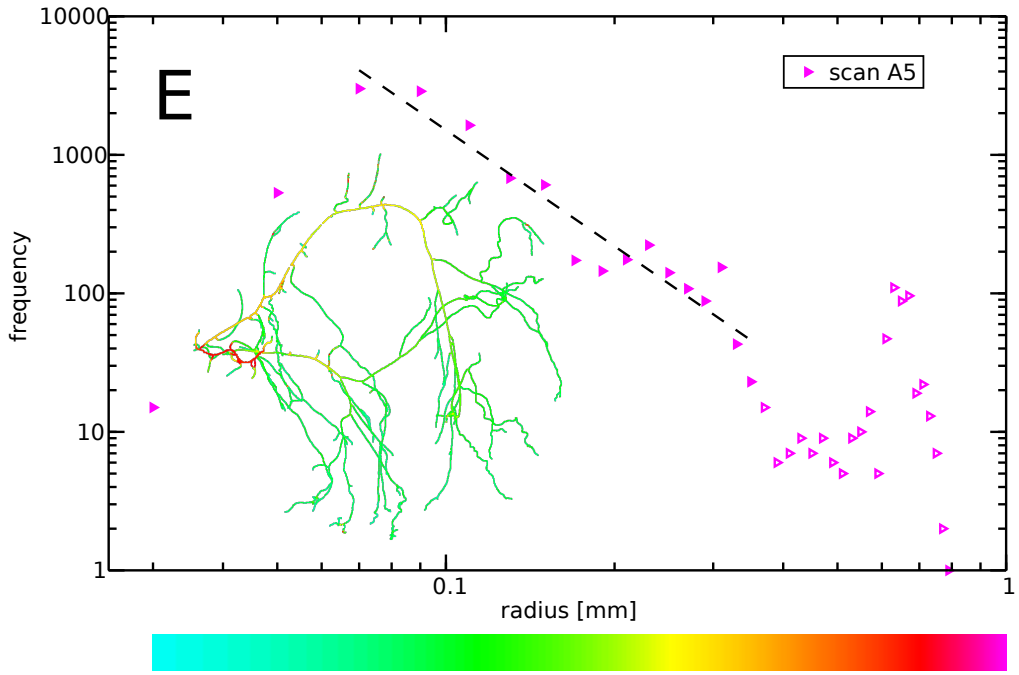

Figure S6: Size Distribution of Cardiac Vasculature (Atria) *(continued).*

E $\alpha = -2.79 \pm 0.25$ Color bar indicates radius from 0.03 to 1 mm. Open symbols indicate data that do not belong to the atrial vasculature.

Section 4) Activation time measurements

We recorded activation wave patterns produced by well-spaced LEAP pulses (interval > 400 ms). We confirmed reproducibility by recording three activation patterns for each field strength. Isochrone maps show the time when the optical signal reached 50% of full action potential amplitude (interpolated to achieve sub-frame precision). Histograms were computed from the isochrone maps and the activation time $\tau(E)$ was computed as the range from the 1st to the 99th percentile of times: $\tau(E)$ = T(0.99) - T(0.01).

The scaling exponents $\tau(E) \propto E^{\beta}$ were estimated using a least square fit. The mean exponent for all atrial preparations (N=3) is $\beta_{atrium} = -0.81 \pm 0.23$ and for all ventricular preparations (N=6) is $\beta_{ventricle} = -0.75 \pm 0.18$ (see Tab. 1). The activation times for individual atrial and ventricular preparations are shown in Figs. S8 und S9, respectively, and the

corresponding exponents β are summarized in Tables S3, S4 and Fig. S7. Statistical analysis showed no significant difference in the exponents β for atria and ventricles (P>0.05).

Preparation	$\beta_{ventricle}$ [mean ± standard error]
#1	-0.76 ± 0.09
#1	-0.78 ± 0.06
#2	-0.35 ± 0.10
#2	-0.97 ± 0.10
#3	-1.08 ± 0.41
#4	-0.92 ± 0.06
#4	-0.54 ± 0.08
#4	-0.94 ± 0.07
#4	-0.68 ± 0.08
#4	-0.90 ± 0.07
#4	-0.55 ± 0.07
#5	-0.67 ± 0.08
#5	-0.55 ± 0.05
#5	-0.81 ± 0.12
#5	-0.67 ± 0.07
#5	-0.83 ± 0.09
#5	-0.64 ± 0.03
#6	-0.99 ± 0.07
#6	-0.53 ± 0.09
#6	-0.87 ± 0.10
#6	-0.67 ± 0.09
#6	-0.80 ± 0.08
#6	-0.64 ± 0.10
$\overline{\beta_{ventricle}}$	**-0.75 ± 0.18**

Table S3: Activation Time Scaling Exponents (Ventricle). The scaling exponent $\overline{\beta_{ventricle}}$ is the weighted average over 23 measurements in N=6 ventricular preparations.

Preparation	β_{atrium} [mean ± standard error]
#1	-0.80 ± 0.06
#1	-1.38 ± 0.09
#1	-0.45 ± 0.11
#1	-0.98 ± 0.10
#2	-0.77 ± 0.06
#2	-0.81 ± 0.05
#2	-0.95 ± 0.08
#2	-0.80 ± 0.08
#2	-1.01 ± 0.08
#2	-1.12 ± 0.10
#3	-0.89 ± 0.05
#3	-0.76 ± 0.05
#3	-0.71 ± 0.05
#3	-0.75 ± 0.03
#3	-0.58 ± 0.03
#3	-0.56 ± 0.04
#3	-0.53 ± 0.03
$\overline{\beta_{atrium}}$	**-0.81 ± 0.23**

Table S4: Activation Time Scaling Exponents (Atria). The scaling exponent $\overline{\beta_{atrium}}$ is the weighted average over 17 measurements in N=3 atrial preparations.

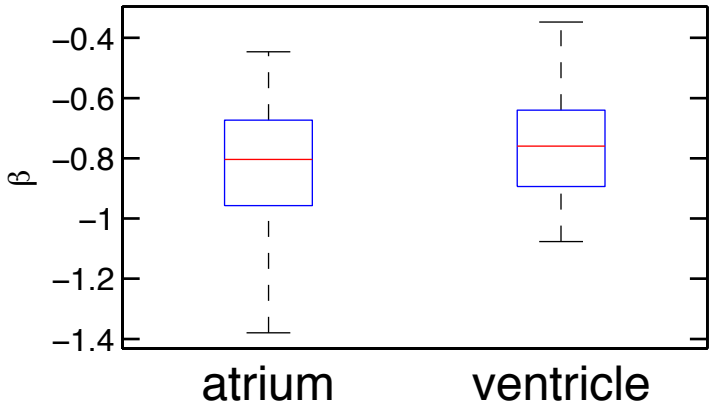

Figure S7: Activation Time Scaling Exponents β for Atrium and Ventricle. The box plot shows median, the 25th and 75th percentile. The whiskers indicate the statistically significant data range. Statistical analysis showed no significant difference in the scaling exponents for atria and ventricles (P=0.31).

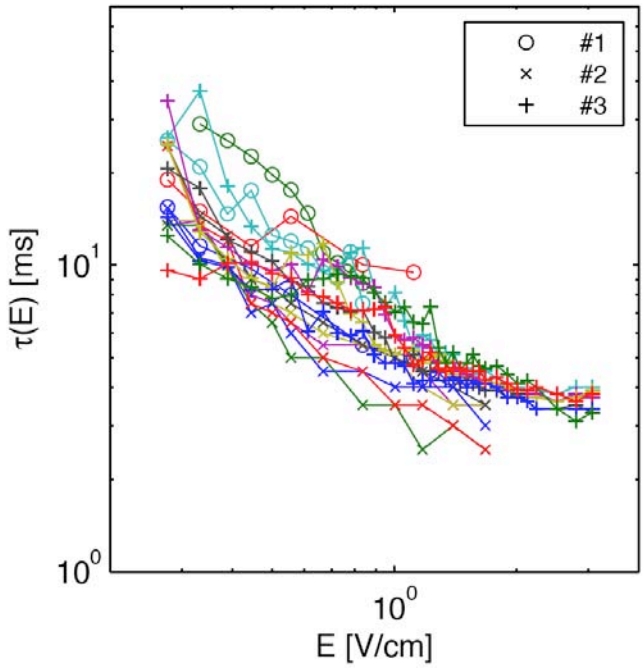

Figure S8: Activation Time Measurements (Atrium). The symbols (circle, cross, plus) indicate N = 3 atrial preparations, colors indicate the 17 measurements of activations times. The corresponding scaling exponents β_{atrium} are obtained from list square fits and are summarized in Table S4.

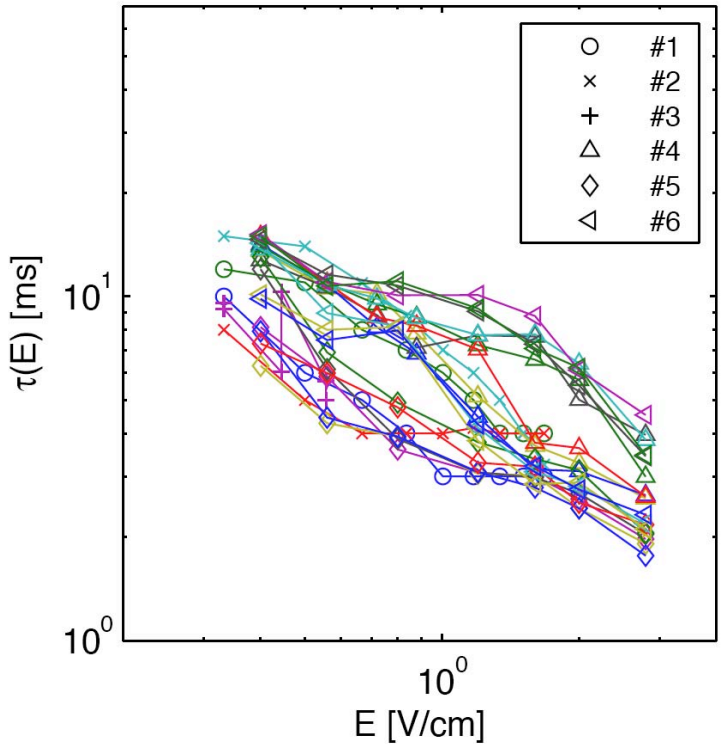

Figure S9: Activation Time Measurements (Ventricle). The symbols (circle, cross, plus, triangle, diamond, left-pointing triangle) indicate the N = 6 ventricular preparations, colors indicate the 23 measurements of activation times. The corresponding scaling exponents $\beta_{ventricle}$ are obtained from least square fits and are summarized in Table S3.

Section 2) Direct Access to the Core

Preparation	Tissue	f_v (Hz)	f_{lEAP} (Hz)
#1	A	7.0 ± 0.1	5.6
#2	A	14.1 ± 0.1	11.8
#2	A	10.0 ± 0.1	8.3
#3	A	14.3 ± 0.1	11.8
#3	A	14.3 ± 0.1	13.3
#4	A	14.9 ± 0.1	10.9
#5	V	8.8 ± 0.1	6.7
#5	V	8.3 ± 0.1	6.7
#5	V	9.0 ± 0.1	6.7

Table S5: Direct Access to Vortex Cores.

Successful termination of fibrillation in N = 4 atrial (A) and N = 1 ventricular (V) preparations *in vitro* with $f_{LEAP} < f_v$, where f_{LEAP} and f_v are the frequency of LEAP and the dominant frequency of fibrillation, respectively. Successful termination of fibrillation with $f_{LEAP} < f_v$ evidences direct access to the core (c.f. Fig. 4, S10, S11). A single pulse at the same energies did not terminate fibrillation. In the episode reported for preparation #4, fibrillation did not terminate immediately but within 1s following LEAP.

It is important to mention that during far field pacing, not only the internal virtual electrodes produced by the heterogeneities of the vesicular structure can produce activations, but that activations can be observed from the boundaries, and depending on the polarity of the field the effect of boundaries can become also important in the amount of tissue excited and thus the effectiveness for termination as shown in Ref (25) of the manuscript. In our case since we use biphasic pulses in the in vivo preparations, the maximum boundary effect was utilized in addition to the internal virtual electrodes.

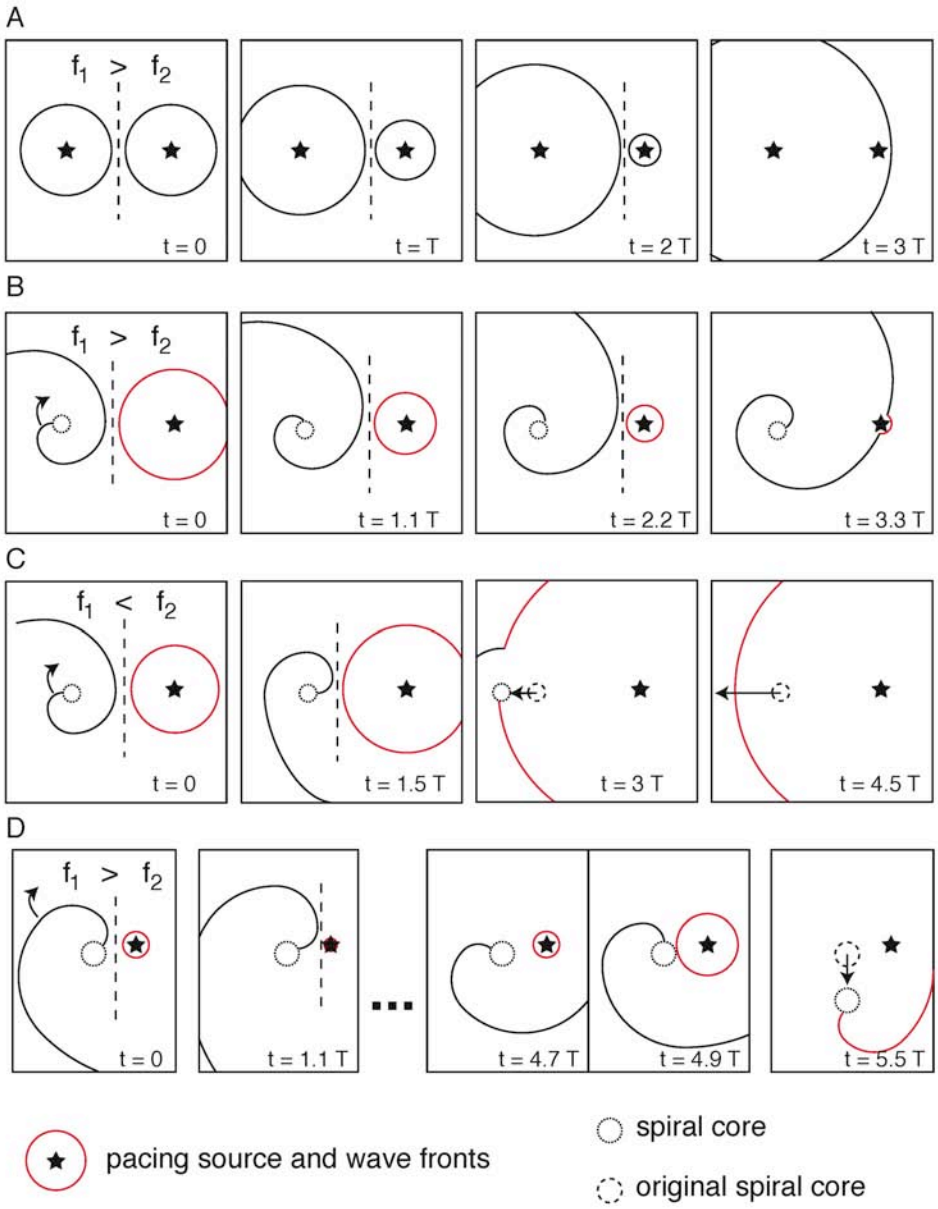

Figure S10: Direct Access to Vortex Cores.

A Schematic of periodic wave emission from distant point-like sources s_1 and s_2 at frequencies f_1 and f_2, where $f_1 > f_2$. Solid lines indicate the positions of wavefronts at times t. The time unit T is the period of a free spiral (c.f. panels D-F). The gray shaded area indicates the region oscillating with frequency f_1. Waves from the high frequency source s_1 progressively entrain the entire region, while waves from lower frequency source s_2 cannot reach the higher frequency

source s_1. The dashed line shows the approximate position at which waves collide (see movie S6).

B The same as in panel A, but the higher frequency source s_1 is replaced here by a spiral wave with the same frequency f_1 (period T). Wavefronts of a free spiral wave (solid black line) rotating with frequency f_1 (period T) in a clockwise direction (indicated by arrow) around a circular spiral core (dotted line). Red solid lines indicate the position of wavefronts originating from s_2 (frequency f_2 with $f_1 > f_2$) and the dotted circle indicates the spiral core (see movie S7). Waves from the higher frequency spiral wave (gray shaded area) progressively entrain the entire region. Waves from the lower frequency source s_2 cannot perturb the spiral wave.

C Same as in panel A, but now the lower frequency source is a spiral wave (frequency f_1). Successive waves from the pacing source eventually reach the core of the spiral and cause it to drift towards the boundary, where it is annihilated (initial core position shown as dashed circle). See movie S8.

D Same as in panel B, except the slower pacing source has been moved closer to the spiral core. The waves from the slower pacing source can reach the spiral core but only if they are emitted during a small time window in the spiral wave's rotation. Thus many cycles may pass during which the pacing source waves cannot reach the core before this window is found and a wave from the pacing source reaches the spiral core, causing a displacement in the core's position. These images were magnified slightly for better illustration. See movie S9.

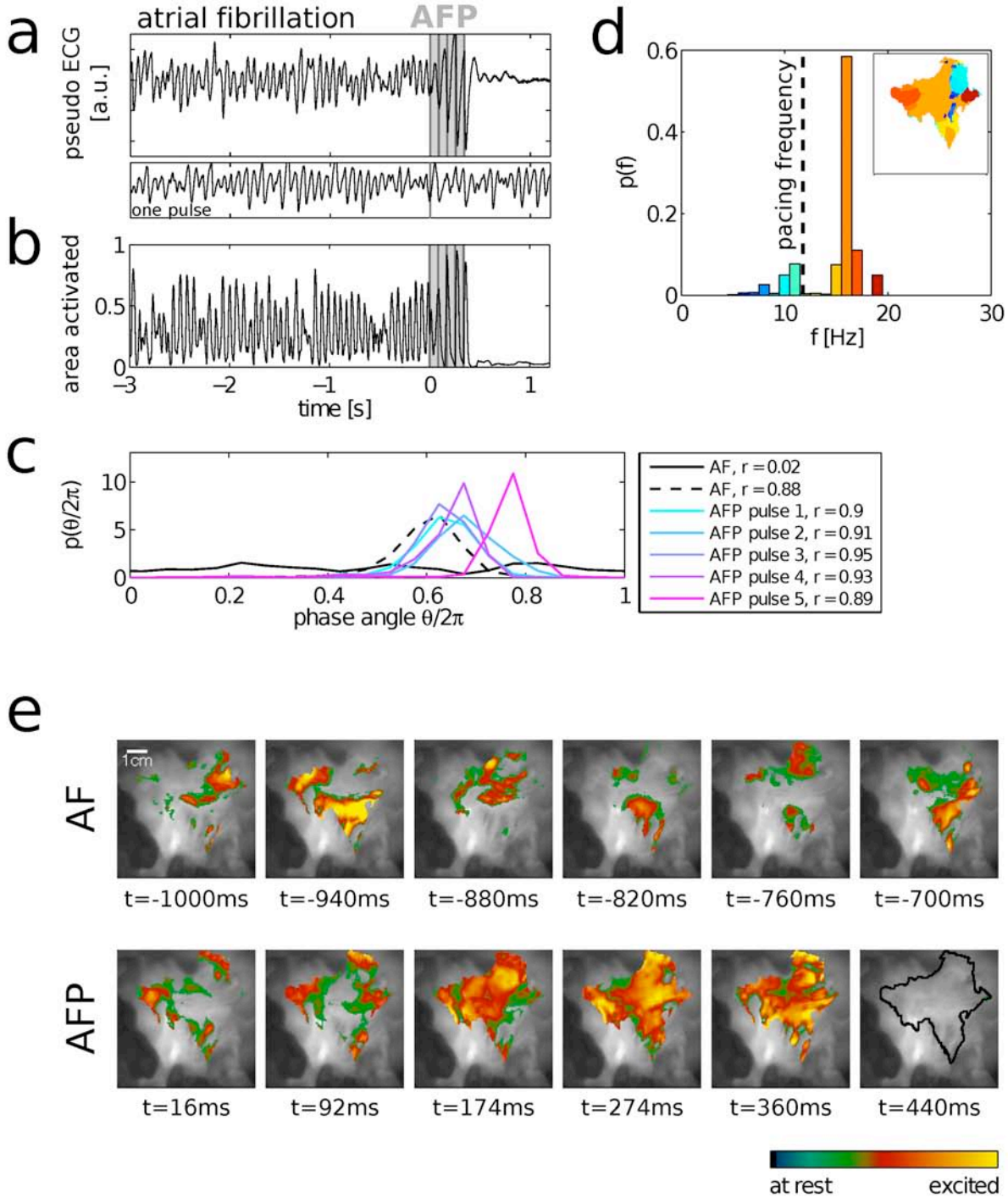

Figure S11: Direct access to vortex cores.

a Termination of atrial fibrillation (AF) with LEAP. The pseudo ECG is obtained from the optical mapping experiments, see SI for details. The vertical gray lines indicate the times at which 5 LEAP pulses (f = 11.8 Hz, electric field strength E = 1.12 V/cm) were delivered. A single pulse

at this field strength did not terminate fibrillation (pseudo ECG below panel A). Following LEAP the signal returns to its resting value, indicating the termination of fibrillation before normal rhythm is resumed. The termination of AF with $f_{LEAP}<f_v$ was observed in atria (N=3, 5 episodes) and ventricles (N=1, 3 episodes).

b Area activated, defined as the fraction of tissue with an optical signal above a certain threshold, indicates tissue synchronization during LEAP. Gray lines indicate times at which LEAP is applied. The threshold value was chosen separately for AF and LEAP to account for differing action potential amplitudes and was defined as the mean optical signal plus half a standard deviation.

c Probability distribution of phases θ_j (Eq. S2) for two times during AF and for the times of strongest synchronization (maximum order parameter r) after each pulse. The corresponding r values are indicated in the legend. During AF, phases are broadly distributed, corresponding to partial coherence. Small perturbations during LEAP induce a transition to a synchronized state corresponding to the termination of AF.

d Probability distribution of dominant frequencies during AF obtained from optical mapping. The dominant frequency map (inset) shows a complex spatial domain structure corresponding to multiple interacting waves using the same color code used for the histogram.

e Spatio-temporal dynamics during AF and LEAP. The field of view is 70 x 70 mm^2. The grayscale image shows the atrium. The snapshots during LEAP are taken at the times of maximum area activated after each pulse (c.f. panel B). The last picture shows quiescence after the termination of fibrillation.

Section 3) Synchronization and Phase Coherence

In order to quantify the observed dynamical states and their response to small perturbations during LEAP, we consider cardiac tissue as an extended system of diffusively coupled oscillators with phases θ_j. We define order parameters r and ψ as

$$re^{i\psi} = \frac{1}{n}\sum_{j=1}^{n} e^{i\theta_j}, \qquad \text{(S2)}$$

where r represents the phase-coherence of an ensemble of n oscillators, and ψ indicates the average phase[S1]. In the incoherent state, the phases θ_j are uniformly distributed in the interval $[0, 2\pi]$ and $r = 0$ (for $n \to \infty$). The fully (globally) synchronized state corresponds to $r = 1$, where all oscillators share a common frequency and phase. In the example shown in Fig. S11 C, the broad distribution of phases θ_j together with an average value for $r = 0.28 \pm 0.16$ (mean ± std) indicate partial coherence during AF. Following the LEAP pulses, the entire tissue converges rapidly to a fully synchronized state, evidenced by the narrow distribution of phases θ_j and the phase coherence approaching unity ($r = 0.97$).

Section 4) Anatomical Structures

We have characterized epicardial anatomical structures in atria and ventricles including pectinate bundles and trabeculae. Figure S12 demonstrates that the structures involved are of size of the order of the millimeter (~2 mm in the atrium, and ~3 mm in the ventricle). Thus, these structures play an important role in the response of the tissue to the field already at very low applied electric fields. However, increasing the electric field past a value of E ~ 0.2 V/cm does not recruit any more of the corresponding discontinuities. Consequently, the response at large electric fields is dominated by smaller structures, such as the one shown due to the vascular structure (c.f. Fig. 3 and S5-6).

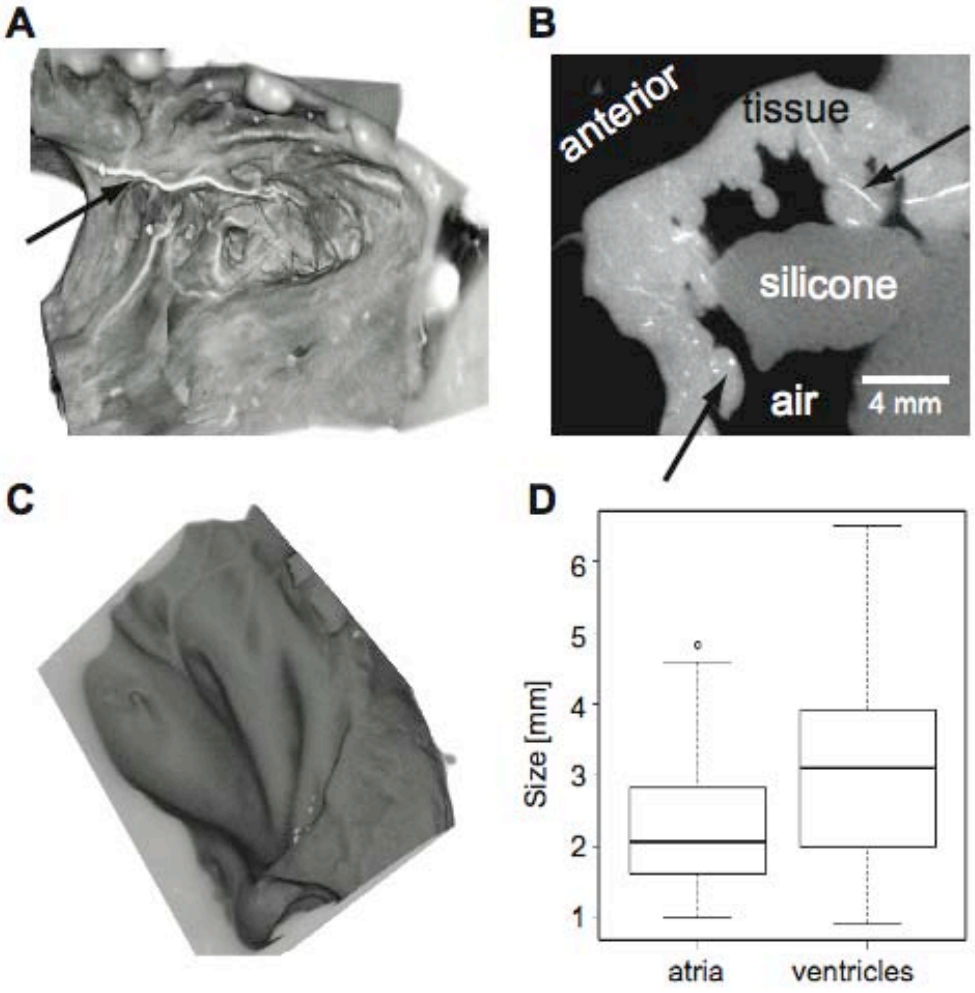

Figure S12: Endocardial Anatomical Structures. **A** Endocardial surface of the right atrial appendage. Vasculature appears bright due to contrast enhancing agent (arrows). **B** Cross section through the micro-CT data shown in panel A. Vasculature appears bright. Data not processed. **C** Left ventricular endocardial surface. **D** The characteristic size of endocardial structures in atria is ~ 2 mm (N=3 preparations) and ventricles ~ 3 mm (N=3 preparations). The box plot shows median, the 25th and 75th percentile. The whiskers indicate the statistically significant data range; circles mark outliers.

Statistical Analysis. Data shown in Fig. 1D were analyzed using an ANOVA, following a log transformation to balance variances. Levene's test confirmed that after log transformation the variances between the groups appeared equal (p-value for inequality post-transformation =

0.4609). A Tukey correction for multiple comparisons was applied and P-values <0.05 were considered statistically significant. In the box plots (Fig. 1D) data points are marked as outliers by red crosses, if they are larger than $w_h = q_3 + 1.5(q_3 - q_1)$ or smaller than $w_l = q_1 - 1.5(q_3 - q_1)$, where q_1 and q_3 are the 25th and 75th percentiles, respectively. The whiskers w_h and w_l correspond to approximately ±2.7 standard deviations (99.3% coverage), if the data are normally distributed. The box plots (Fig. 1d) show the median and the 25th and 75th percentiles. The whiskers indicate the statistically significant data range and red crosses mark outliers

Section 5) Supplementary Equations

Solution of Equation 1. With the help of Eq. 1 from the main text, we can estimate the effect of an electric field on the membrane potential near non-conducting regions of tissue. For this purpose, we model blood vessels as infinitely long cylinders. This is a good approximation, as long as the blood vessels do not curve considerably within a distance of a few λ. As the solution must be translational invariant along the centerline of the cylinder, Eq. 1 reduces to a two-dimensional problem for a circle. We also assume that the electric field vector is perpendicular to the centerline of the cylinder (in reality, only the component perpendicular to the centerline is of interest).

The two-dimensional solution of Eq. 1, which is appropriate for our physical problem, has a dipolar symmetry ($e = e(r)\cos\theta$, where θ is the angle with respect to the direction of the applied electric field). With this ansatz, Eq. 1 reduces to the following ordinary differential equation for the radial dependence of e:

$$\frac{d^2e}{dr^2} + \frac{(d-1)}{r}\frac{de}{dr} - \left(\frac{1}{\lambda^2} + \frac{(d-1)}{r^2}\right) e = 0 . \qquad \text{(S3)}$$

With the physiological constraint that $e(r) \to 0$ as $r \to \infty$, the solution to the above equation is a hyperbolic Bessel function of the second kind

$$e(r,\theta) = \lambda E(K_1(r/\lambda))/(K_1'(R/\lambda))\cos\theta , \qquad \text{(S4)}$$

where R is the radius of the obstacle[S2]. The maximum depolarization is reached in the direction anti-parallel to the electric field ($\theta = \pi$) at the boundary of the heterogeneity ($r = R$). A

heterogeneity is assumed to be activated as a wave source, if the depolarization exceeds a threshold value $\Phi_t - \Phi_{rest}$. With the help of Eq. (S4), one finds that the electric field strength needed to induce a depolarization of $\Phi_t - \Phi_{rest}$ is

$$E = -\frac{\Phi_t - \Phi_{rest}}{\lambda} \frac{K_1'(R/\lambda)}{K_1(R/\lambda)}. \tag{S5}$$

This function, shown in Fig. S13, gives the electric field strength needed to recruit a heterogeneity of size R as a wave source.

For small heterogeneities (small radii), the electric field (see Fig S13) is inversely proportional to the radius (E ~ 1/R). Defining, as in the main text, $R_{\min}(E)$ as the size of the smallest obstacles that emit waves when an electric field of strength E is applied, if follows from the relation above that:

$$R_{\min}(E) \approx \frac{1}{E} \tag{S6}$$

Activation Time Prediction from Structural Data. Knowing the function $R_{\min}(E)$, geometric considerations make it possible to predict the activation time (time to full activation) from the size distribution of heterogeneities in the tissue. We model the wave sources activated by the electric field as point sources. In homogeneous tissue, an excitation wave propagating radially from a single site excites in a time τ a volume $V(\tau)$:

$$V(\tau) = \alpha \cdot \pi \left(v\tau\right)^d \tag{S7}$$

where v is the velocity of the wave, d is the dimension of the tissue (d = 2 for atrial tissue, d=3 for ventricular tissue) and $\alpha = 1,\ 4/3$ for $d = 2, 3$. The amount of tissue excited by N_s sources uniformly distributed in the tissue is simply $N_s \times V(\tau)$. As a consequence, the time it takes to excite the full volume V can be estimated from the condition

$$N_s \times V(\tau) = V \tag{S8}$$

(the equation above neglects the overlap between regions excited by several sources). Introducing the density of wave sources

$$\rho = N_s / V \,, \tag{S9}$$

the condition for activation of all the tissue, Eq. (S8), is equivalent to:

$$V(\tau) = \rho^{-1} \tag{S10}$$

The activation time is related to the structural features of the tissue via the wave source density, a function of the electric field of strength E. This can be deduced from Eq. (S5), which provides an expression for the minimum electric field necessary to emit a wave from a heterogeneity of size R: for a given value of E, heterogeneities of size larger than $R_{\min}(E)$ emit a wave.

Assuming a random distribution of heterogeneities, uniformly distributed in the system, such that the number of heterogeneities whose size R is in the interval $R' \le R \le R' + \Delta R'$ is $N \times p(R')\Delta R'$, where N is the total number of heterogeneities in the system, the number of heterogeneities that will emit waves when the tissue is stimulated by a field of strength E is:

$$N(E) = N \int_{R_{\min}(E)}^{R_{\max}} p(R)\, \mathrm{d}R \,, \tag{S11}$$

where $R_{\max}$ is the largest size in the tissue. This leads to a density of wave sources, $\rho(E) = N(E)/V$

$$\rho(E) = \frac{N}{V} \int_{R_{\min}(E)}^{R_{\max}} p(R)\, \mathrm{d}R \,, \tag{S12}$$

Thus, the condition for the time necessary to activate the tissue is given, see Eq. (S7), by $V(\tau) = \rho(E)^{-1}$ which can be simply re-expressed as

$$\tau^d(E) = \left(\alpha \pi v^d \frac{N}{V} \int_{R_{\min}(E)}^{R_{\max}} p(R)\, \mathrm{d}R \right)^{-1} . \tag{S13}$$

This equation was used in Fig. 3 to predict activation times from a given heterogeneity size distribution (with $d = 2$ for atria and $d = 3$ for ventricles). The predictions from structural data

(Fig. 3c, 3d, 3g and 3h) are only known up to a constant factor (composed of N and V) and were scaled arbitrarily to fit the experimentally measured activation time data.

If $p(R)$ is assumed to follow a power law $p(R) \propto R^{-\alpha}$, then using equations (S6) and (S13), the time of activation will also follow a power law of the form:

$$\tau(E) \propto E^{-(\alpha-1)/d}$$

This equation is used to convert power law exponents from size distributions to a power law for the activation times throughout the paper. A fixed small number of wave sources – assumed to be large and thus indiscriminately activated at all considered field strengths – was added to the source density to account for large objects not captured by blood vessel detection (tissue boundaries, endocardial structure, etc).

The values used for Eq. (S5) were $\Phi_t - \Phi_{rest}$ = 15 mV and λ = 1 mm.

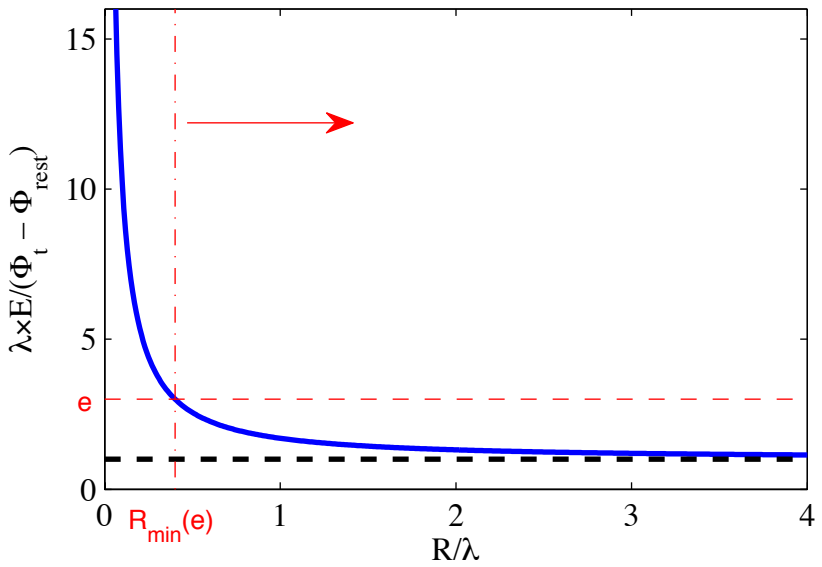

Figure S13: The relation between the size *R* of the heterogeneity and the electric field required to emit a wave. The exact mathematical formula is given by Eq. S5. As shown here, this curve enables us to determine the smallest size $R_{min}(e)$ of heterogeneities that may emit waves: given a value of e, the intersection between the curve and horizontal red dashed line defines the value $R_{min}(e)$. Any obstacle of size $R > R_{min}(e)$ – right of the dashed-dotted line,

indicated by the arrow – will fire when a field e is applied. The horizontal dashed black line indicates the minimum field strength for which *any* heterogeneity will be recruited as a wave source.

Role of Homogeneity and Isotropy. The assumption of homogeneous source distribution depends on the characteristic size of the vessel. Whereas at the smallest available scale (e.g. the diffusive length scale corresponding to arterioles) the distribution is homogeneous, as required to properly supply nutrients throughout the entire tissue, the spatial distribution becomes progressively inhomogeneous towards larger scales, reflecting the arborizing vascular architecture. Consequently, we observe an increasing variability of activation times at low field strengths.

The assumption of isotropic conduction velocity does not limit our findings, as we are primarily interested in the scaling behavior of the activation times, which does not depend on the anisotropy ratio.

Section 6) Clinical Implementation

We point out that prior to clinical implementations of our approach for atrial arrhythmias, several technical issues will need to be addressed, including the possibility of LEAP inducing VT/VF. Accordingly, we expect that the use of LEAP in clinical settings will require protocols that avoid the delivery of LEAP during the ventricular vulnerable window.

Section 7) Supplementary Videos

S1 Video showing atrial fibrillation (AF) and successful termination of AF (see Fig. 1c and e). The color indicates membrane potential (black = resting, red activated; c.f. color bar given in Fig. 1e). The times of the five LEAP pulses are indicated by a red square. The field of view is 4 x 4 cm^2. Note that during LEAP, waves originate both from boundaries and form inside the tissue.

S2 Video showing normal sinus rhythm (see Fig. 1e). The color indicates membrane potential (black = resting, red activated; c.f. color bar given in Fig. 1e). The field of view is 4 x 4 cm^2.

S3 Videos showing representative examples of wave propagation in quiescent tissue induced by weak electric field pulses with E = 0.22 V/cm, E = 0.39 V/cm and E = 0.5 V/cm, respectively (pulse duration 8 ms). The color indicated time (early = red, late = blue; see Fig. 2).

S4–S7 Videos showing simulations corresponding to Figure S10, panels A–D. The simulations have been done using the Barkley model. The color indicates the fast activator variable (blue = resting, red = activated). The text at the beginning of each video indicates pacing sites and relative frequencies. During the simulations, phase singularity trajectories are tracked where appropriate (indicated by white color).

S8 Video showing AF and successful termination using direct access to the core (Fig. 4e). The color indicates membrane potential (black = resting, red activated; c.f. color bar given in Fig. 4d). The times of the five LEAP pulses are indicated by a red square. The field of view is 4 x 4 cm^2.

S9 3D interactive Applet for the right atrial vessel structure shown in Fig. 3b. http://thevirtualheart.org/vessels/atria/Right_atria_vessels.html

S10 3D interactive Applet for the left ventricular vessel structure shown in Fig. 3f. http://thevirtualheart.org/vessels/ventricle/vessels1a.html

Section 8) Detailed contribution of the authors.

Initials are listed in alphabetical order.

EB, FHF, RFG, VK, SL, and AP initiated the research program, formulated the aims of the research, and participated in all parts of the conceptual, theoretical and experimental analysis and writing of the manuscript.

PB, EB, FHF, RFG, DH, SL, AS participated in the analysis of the data.

PB, EB, FHF, RFG, DH, VK, SL, AS, AP, and MZ participated in the interpretation of the data.

PB, SL, and AS designed and built the optical mapping system.

EB, FHF, RFG, VK, and SL participated in the conceptual design to analyze the optical mapping data.

PB, FHF, SL, and AS designed the software to analyze the optical mapping data.

PB, FHF, SL, and AS carried out the in vitro optical mapping experiments.

PB, FHF, SL, and AS processed and analyzed the optical mapping data.

FHF, RFG, and AS prepared samples for the in vitro experiments.

FHF, RFG, GH, BK, VK, SL, and MZ participated in the design of the in vivo experiments.

LC, FHF, JF, RFG, AG, BK, SL, and AS prepared the in vivo experiments

FHF, RFG, BK, SL, AS, and MZ carried out in the in vivo experiments.

FHF and SL processed and analyzed the in vivo data.

PB, FHF, and AS prepared samples for CT scanning.

PB, DH, GL, and SL analyzed the structural data (micro-CT) and acquired the vessel size distributions.

PB, EB, EMC, FHF, RFG, VK, SL, AP, and AS participated in the conceptual design to link structural (micro-CT) to functional (activation time) data.

PB, FHF, DH, and SL designed and implemented the numerical method to link structural (CT) to functional (activation time) data.

PB, EB, EMC, FHF, RFG, VK, SL, AP, and AS participated in the development of the theoretical concepts.

PB, EB, EMC, FHF, RFG, DH, VK, SL, AP, AS, and MZ participated in writing the manuscript.

Section 9) Supplementary References

S1 Kuramoto, Y., Chemical Oscillators, Waves and Turbulence, Springer Berlin (1984)

S2 Abramovitz, M. and Stegun, I.A., Handbook of Mathematical Functions, Dover New York (1972)